Lithium Ion Conductivity of a Statically and Dynamically Compacted Nano-structured Ceramic Electrolyte for Li-Ion Batteries

M.J.G. JAK, E.M. KELDER, & J. SCHOONMAN

Laboratory for Applied Inorganic Chemistry, Delft University of Technology, Julianalaan 136, 2628 BL, Delft, The Netherlands

N.M. VAN DER PERS

Department of Physical Chemistry of the Solid State, Delft University of Technology, Rotterdamseweg 137, 2628 AL, Delft, The Netherlands

A. WEISENBURGER

Forschungszentrum Karlsruhe, Technik und Umwelt, Institut für Neutronenphysik und Reaktortechnik, P.O. box 3640, D-76021, Karlsruhe, Germany

Abstract. The densification of a ceramic electrolyte for rechargeable lithium ion batteries by using different compaction methods is described. The ceramic electrolyte for lithium ions, BPO_4- Li_2O, is compacted using either static or dynamic compaction methods. A difference in peak width in the X-ray diffraction spectra and a difference in lithium ion conductivity is observed. The dynamically compacted BPO_4-Li_2O shows an increase of up to three orders of magnitude in total ionic conductivity as compared with statically compacted samples. The total lithium ion conductivity is up to 2.10^{-4} S/cm at room temperature, which can compete with polymer electrolytes.

1. Introduction

The advantages of Li-ion batteries such as high energy density, high cell voltage, and cycleability outclass conventional battery systems [1]. The market potential of Li-ion batteries has resulted in a widespread interest in the materials research of components for Li-ion batteries and to date a large number of publications has appeared. The majority of these papers deal with battery systems based on intercalation compounds for both anode and cathode separated by a liquid or polymer-based electrolyte. Instability of these electrolytes, caused by high battery voltages, causes capacity fade and a decrease in cycle life. Decomposition of the electrolyte often results in gas evolution leading to irreversible processes and high pressures which may be detrimental to the battery [2–4].

With regard to the variety of liquid and polymer-based electrolytes only a few ceramic electrolytes have been studied [5–14]. In addition, most of these solid electrolytes contain exotic and/or expensive metallic species and the lithium ion conductivity at room temperature is significantly lower than that of the liquid and polymer-based electrolytes [15]. In a previous paper [5] we reported on a new lithium ion conducting ceramic electrolyte, BPO_4-Li_2O, which can be synthesized using a very simple synthesis route and commercially available precursor compounds.

A disadvantage of using only ceramic battery components is the usual poor electrical contact between electrode and electrolyte, thus leading to high interface resistances. The contact areas may be improved by using high temperatures and/or high pressures. The use of high temperatures may lead to interface reactions, decomposition, melting,

segregation, and grain growth of the components. Therefore, our research focuses on the use of high pressure pulses, also referred to as dynamic compaction.

2. Experimental

The synthesis of BPO_4-$0.035Li_2O$ via the boric acid and a phosphoric reactant synthesis route is described in [5]. The result of these syntheses is a ceramic foam of Li-doped BPO_4 with a very low density. In order to decrease the volume, a slightly different synthesis is used in the present study and is described below.

Phosphoric pentoxide (P_2O_5), boric acid (H_3BO_3), and lithium hydroxide mono hydrate ($LiOH \cdot H_2O$) are weighted in proper amounts according to the following reaction:

$$P_2O_5 + 2H_3BO_3 + 0.14\ LiOH \cdot H_2O$$
$$= 2\ BPO_4 \cdot 0.035Li_2O + 3.21\ H_2O \quad (1)$$
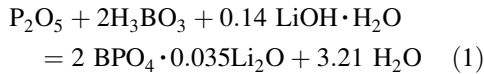
As a result BPO_4 with 7 mole% Li is obtained. In [5] it is shown that BPO_4 with 7 mole% Li exhibits the highest lithium ionic conductivity. P_2O_5, H_3BO_3, and $LiOH \cdot H_2O$ are mixed in a Pyrex beaker with CO_2-free de-ionized water until a homogeneous paste is formed. Subsequently, the beaker is covered with

aluminum foil with a few small holes and placed in a programmable oven (NEY 2-525 series II). The following temperature program was used:

– heating from room temperature to 110°C at 1°C/min
– kept at 110°C for 3 h
– subsequent heating from 110°C to 600°C at 5°C/min
– kept at 600°C for 10 h
– cooling down in the oven to room temperature.

The whole synthesis takes place in air. After synthesis, the powders are ball-milled using a planetary micro mill (Fritsch Pulverisette 7) in order to break up the agglomerates down to approximately 10 μm. Subsequently, the powders were compacted by using the following compaction methods:

Dynamically: Explosive Compaction (EXC) [16]
                    Magnetic Pulse Compaction (MPC) [17]
Statically: Cold Uniaxial Pressing (CUP)
                  Hot Uniaxial Pressing (HUP)

The pressure and pressure velocity ranges of the different compaction techniques are gathered in Fig. 1. The EXC as well as the MPC experiments are performed uniaxially. The HUP experiments are performed at 1500°C and a processing time of
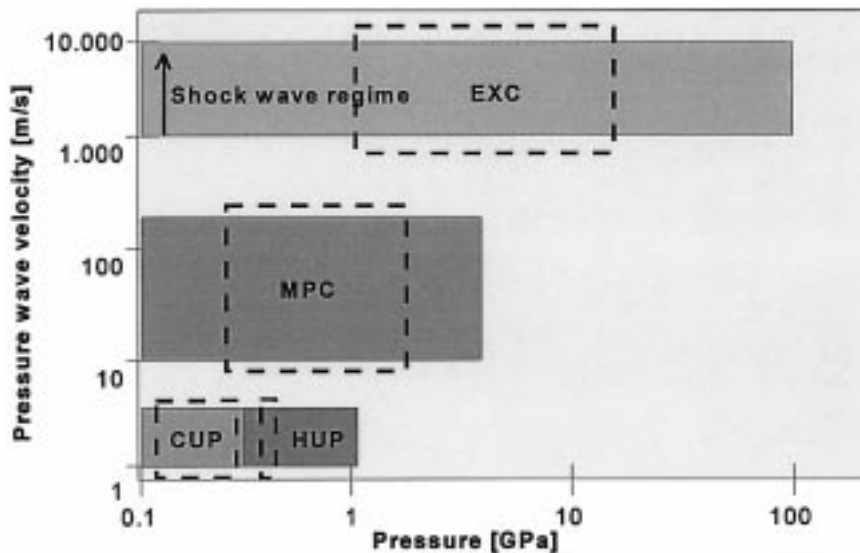

Fig. 1. Different compaction techniques with their typical pressure and pressure velocity ranges. The dotted lines indicate the pressure ranges used in this study.

5 min as the sample is also heated and cooled down. The pressing time for the CUP samples is 10 min.

After compaction the relative density of the samples is determined by measuring volume and weight and dividing by the theoretical mass density (TMD).

Subsequently, the samples were embedded in a polyester resin and polished in order to obtain clean, plan parallel samples with a smooth surface. Prior to the electrical measurements the samples were dried under vacuum at 50°C for at least 2 h. Two different electrical measurement techniques are applied:

1. AC impedance spectroscopy performed with a Schlumberger Solartron 1260 Frequency Response Analyzer, amplitude 50 mV, frequency range from 0.1 to 5.10^6 Hz.
2. DC measurements by applying a block voltage pulse of 50 mV with a potentiostat (EG&G Princeton Applied Research 273). The voltage pulse duration is 60 or 120 seconds, which is equivalent to a frequency of 0.02 or 0.01 Hz, respectively. The selected pulse duration depends upon the time to obtain a constant current.

These two measurement techniques are applied on two different electrochemical cells, i.e.,

Cell I: Pt$^\sharp$|BPO$_4$-Li$_2$O|Pt$^\sharp$

Cell II: Li|separator*|BPO$_4$-Li$_2$O|separator*|Li

$^\sharp$ sputtered, dense Pt electrode (Edwards Sputter Coater S150B).

* separator: Celgard 2500 membrane (Hoechst) filled with a liquid electrolyte of LiBF$_4$ in propylene carbonate (PC).

With Cell I the Li$^+$ conductivity as well as electronic conductivity can be measured using dc pulse measurements. With Cell II however, only the Li$^+$ conductivity is measured in the dc experiments. The experiments on Cell II are performed with the cell placed in an argon filled glove box.

From all the samples compacted with different methods, one representative sample of each compaction method is selected. The compacted samples and the BPO$_4$-Li$_2$O starting powder are investigated with X-ray diffraction (XRD) analysis (Siemens D500 diffractometer with incident beam CoKα_1 monochromator and position sensitive detector). As a reference material a polycrystalline SiO$_2$ powder is used. Prior to the XRD analysis the samples are dried under vacuum for 60 h at 60°C.

Finally, all the samples used for the XRD analysis are investigated with Scanning Electron Microscopy (SEM, Jeol 6400F and Leitz AMR 1000).

3. Results and Discussion

3.1. Starting Material

SEM analysis of the starting powder shows that the material consists of agglomerates of primary particles with a grain size of 50–100 nm (Fig. 2). Particle size analysis (Fritsch Particle Sizer Analysette 22) shows a bimodal agglomerate distribution with agglomerate sizes of 3 and 7 μm. The theoretical mass density (TMD) of 2.906 g/cm^3 is determined from the XRD spectrum of the starting powder. The crystal structure of BPO$_4$ is the high-cristoballite (tetragonal) structure. According to JCPDS 34-132 [18] the TMD of pure BPO$_4$ without Li is 2.805 g/cm^3. According to [18] the pure BPO$_4$ tetragonal material has an a-axis of 4.34253 Å and a c-axis of 6.6415 Å. The BPO$_4$ without Li synthesized with the P$_2$O$_5$ synthesis as described before shows an a-axis of 4.3383 Å and a c-axis of 6.6436 Å. From the XRD spectrum of the BPO$_4$- Li$_2$O (7 mole% Li) starting material an a-axis of 4.3382 Å and a c-axis of 6.6298 Å are determined. The decrease of 0.2% of the c-axis and, hence, an increase of 0.67% in TMD can be explained by incorporation of Li in the BPO$_4$ structure. The a-axis is not influenced upon doping.
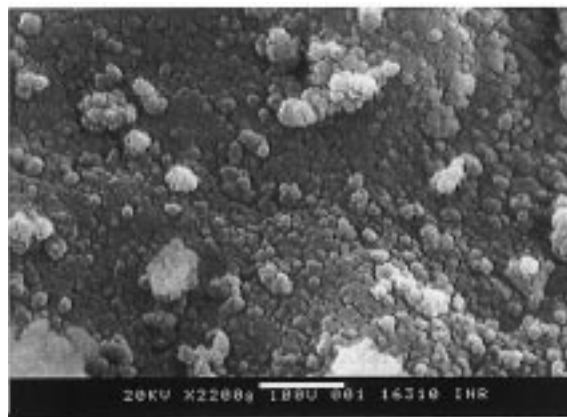

Fig. 2. SEM micrograph of the starting powder (P$_2$O$_5$ synthesis) (bar = 1 μm).

Table 1. Results of BPO_4-Li_2O using different compaction methods (room temperature)

Compaction method	P [MPa]	Diameter [mm]	Thickness [mm]	Density [% TMD]	β [°2θ]	σ_{Li^+} [μS/cm]
Hot Uniaxial Pressing (HUP)	500	9.7	2	94	0.17	0.7–2
Cold Uniaxial Pressing (CUP)	375	8.2	4.4	56	0.29	2–20
Magnetic Pulse Compaction (MPC)	1000	15	2	65	0.48	2–50
Explosive Compaction (EXC)	3500	10	2	70	0.45	80–200
Starting Powder	—	—	—	—	0.47	—
StartingPowder (800°C)	—	—	—	—	0.19	—
SiO_2 reference	—	—	—	—	0.11	—

3.2. Compaction Results

Several results of the densification of BPO_4-Li_2O with different compaction methods are gathered in Table 1. These samples are used for the XRD experiments. From the data in this table it is obvious that the HUP sample has the highest density and the CUP sample the lowest density. The mentioned samples are representative for each method, based on series of experiments performed with each method. In Fig. 3 the final density of BPO_4-Li_2O is depicted as a function of the applied pressure. From this graph it can be concluded that the final density depends not only on the applied pressure, but also on the pressure wave velocity and the compaction temperature. Scanning electron microscopy analysis clearly shows densified areas in the dynamically compacted
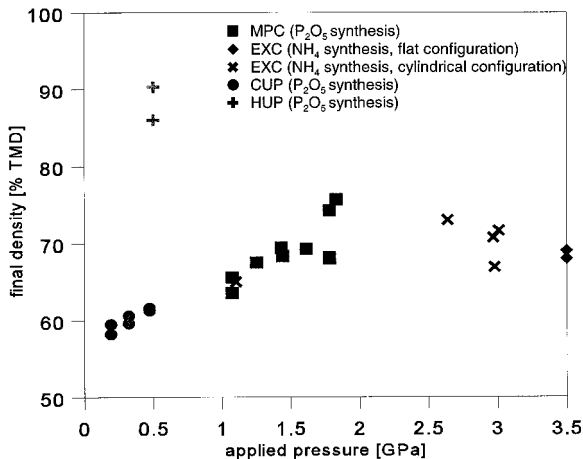
samples and the presence of the nano-structured particles of the starting material (Fig. 4). These clearly densified areas are not observed in the CUP samples. The CUP samples show a grain size of approximately 100–300 nm. The MPC and especially the CUP samples are quite brittle. From this property it can be deduced that the intergranular bonding is poor, which is also supported by the observation that the samples can be powdered easily. This weak intergranular bonding is caused by both the low compaction velocity [19,20] and the low temperature. On the contrary, the EXC and especially the HUP samples show a very good mechanical strength. SEM analysis of the HUP samples shows grain growth of the primary particles (Fig. 5). The grain size varies between about 100 nm and 1000 nm. After HUP the material is still crystalline, which can be deduced from the visible facets of the grains in Fig. 5 and the narrow peaks in the XRD spectrum in Fig. 6.

Fig. 3. Final density as percentage of the TMD as a function of the applied pressure. NH_4 stands for the ammonium synthesized material (foam) and P_2O_5 for the phosphorous pentoxide synthesized material. EXC (flat) means a flat pressure wave, EXC (cylindrical) means a cylindrical pressure wave.

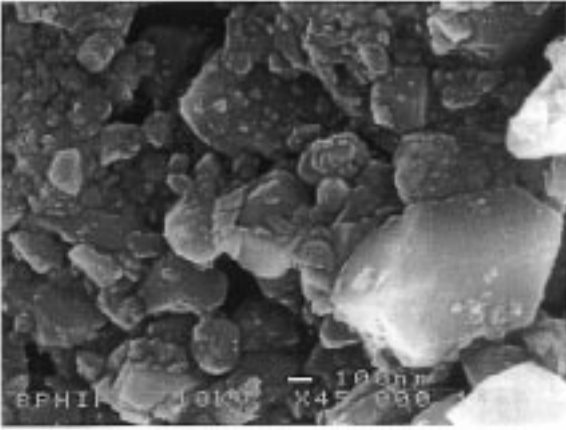*Fig. 4.* SEM micrograph of an MPC sample (pressure 1.8 GPa, density 68% TMD). Box indicates a clearly densified area.

Fig. 5. SEM micrograph of a HUP sample (pressure 0.5 GPa, $T = 1500°C$, density 90% TMD).

3.3. X-Ray Diffraction Analysis

In Fig. 6 the XRD spectra of the samples of each method listed in Table 1 are plotted. Comparison of the XRD spectra with the starting powder spectrum leads to three conclusions:

(a) no peak shift is observed
(b) no additional and/or disappearing peaks
(c) a decrease in peak width of the statically compacted samples

Absence of peak shift and/or additional or disappearing peaks proves that no phase transition took place and/or second phases are formed. Furthermore, macro strain is absent since macro strain also causes a peak shift. The small peak at $2\Theta = 32.5°$ is attributed to a new crystalline phase due to hydration [5]. In order to study the peak width in more detail a slow scan of the $2\Theta = 75.4°$ peak (representing the {213} reflection) is performed (Fig. 7). From these scans it
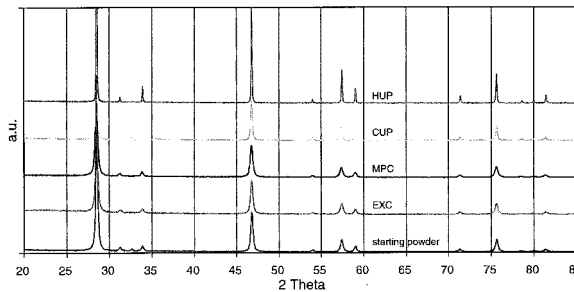

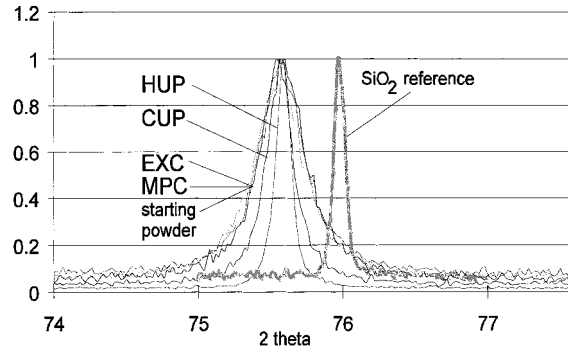Fig. 6. XRD spectra of starting material and compacted samples.

Fig. 7. XRD spectra of starting material and compacted samples. Slow scan of the $2\Theta = 75.4°$ peak ({213} reflection).

is clear that a decrease in peak width of the statically compacted samples compared with the starting powder and the dynamically compacted material took place. The results are quantitatively presented in Table 1 as the integral width β, being the surface of the peak divided by its height.

Peak broadening may be caused by the presence of submicron particles (smaller than approx. 200 nm) and/or lattice defects. The separation of these effects is possible by XRD but outside the scope of this work. The primary particles causing peak broadening are the crystallites consisting of a coherently diffracting domain. With lattice defects one- and more-dimensional defects as well as point defects, inducing local strain, are meant. The local strain will cause peak broadening due to small deviations from the Bragg reflection. The one- and more-dimensional defects are not in thermodynamic equilibrium [21], and will, therefore, disappear upon heating. On the contrary, the point defects are in thermodynamic equilibrium, and will remain upon heating and cooling [21]. In order to study the possible type of defects, a slow scan of the $2\Theta = 75.4°$ peak of the starting powder which is heated at 800°C for 12 h is recorded and reveals a significant decrease in peak width. During the heat treatment sintering takes place, which is observed by an increase in particle bonding. Comparison of the peak width of the heat treated starting powder with the peak width of the SiO_2 reference ({113} reflection, Table 1) indicates that these peak widths are comparable. It is assumed that the as synthesized powder doesn't contain a significant amount of one- and more-dimensional defects, since after the synthesis the powders are cooled down slowly. Therefore,

the amount of point defects in the starting material is probably negligible, and the decrease in peak width is caused by the increase of the primary particle size. A comparison of slightly mortared as synthesized powder and ball-milled starting powder does not show any difference in peak width which indicates that none of the aforementioned defects are generated by the milling process.

The very narrow peaks of the HUP sample (Figs. 6, 7) can be attributed to the effect of the high temperature (1500°C, 5 min, 500 MPa) during the HUP process. Due to this high temperature, most of the one and more-dimensional lattice defects present will disappear and grain growth will occur. This grain growth was already shown in Fig. 5. When comparing the width of the $2\Theta = 75.4°$ peak with the width of the $2\Theta = 76.0°$ peak of the SiO_2 reference, one may conclude that the HUP BPO_4-Li_2O sample has a high crystallinity and exhibits a low defect concentration.

3.4. Electrical Measurements

In Fig. 8 a representative impedance spectrum of Cell I is shown. In order to interpret the impedance spectra, the different processes that occur in the electrochemical cell need to be considered. In Cell I three processes may be distinguished, i.e., bulk conductivity, grain boundary conductivity, and polarization of the interface Pt|BPO_4-Li_2O. From literature [22] it
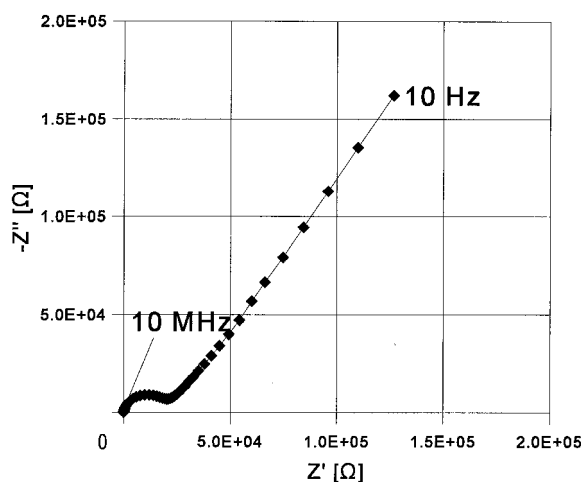
is known that the intercept of the Warburg impedance with the real impedance axis (Z') is the total ionic resistance. This total ionic resistance includes bulk and grain boundary resistance.

The spectra can be fitted with an electrical equivalent circuit containing two parallel branches containing R and Q elements (with R representing a resistor and Q representing a constant phase element) in series with a Warburg-like constant phase element. One of the parallel branches represents the Li^+ grain boundary conductivity and the other branch represents the Li^+ bulk conductivity. The impedance data are simulated by using the data analysis program EQUIVCRT [23]. A detailed impedance spectroscopy study is beyond the scope of this paper and will be published in a forthcoming paper. The dc resistance at room temperature is of the order of 10^8 Ω or higher, indicating a negligibly low electronic conductivity. The ''infinite'' dc resistance shows the absence of a dc conduction path through this cell. Figure 9 shows a representative spectrum of the measurements of Cell II. The possible processes in this cell are: bulk conductivity, grain boundary conductivity, the BPO_4Li_2O|separator interface, and Li|separator interface. Measurements on the cell Li|separator|Li show a dc resistance of only a few Ohms. Therefore, we can neglect the impedance of the interface Li|separator. The spectra of Cell II can be fitted with the two parallel branches as described for Cell I in series with a parallel RQ branch in series. The parallel RQ branch
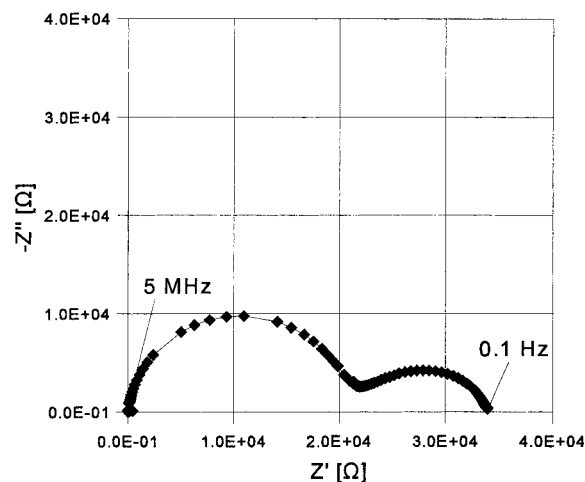

Fig. 8. Representative ac impedance spectra of Cell I: Pt|BPO_4-Li_2O|Pt at room temperature in air. Sample is EXC BPO_4-Li_2O.

Fig. 9. Representative ac impedance spectrum of Cell II: Li|separator|BPO_4-Li_2O|separator|Li at room temperature under argon. Sample is EXC BPO_4-Li_2O.

in series represents the BPO_4|separator interface. dc measurements show a similar resistance compared with the extrapolated resistance at the low-frequency end of the impedance spectra. The finite dc resistance shows the dc conduction path for Li^+ through this cell. Comparison of the dc resistance of Cell II with the intercept of the Warburg of Cell I shows a slightly higher value. The difference between the two total resistances is caused by the contribution of the interface BPO_4Li_2O|separator. The contribution of the interface BPO_4-Li_2O|separator is supported by the observed increase of one of the semi-circles in time due to evaporation of the liquid electrolyte in the separator. From the similarity of the results it can be concluded that the electronic resistance is negligible and, therefore, the Li^+ conductivity is measured with Cell I.

In Table 1 the results of the total Li^+ conductivity (σ_{Li^+}) of the different BPO_4-Li_2O samples at room temperature are included. The total ionic conductivity is specifically used since this parameter is relevant for Li-ion batteries. From Table 1 it can be concluded that the total ionic conductivity of the dynamically compacted samples is significantly higher than that of the statically compacted samples. The differences in Li^+ conductivity as a result of the different methods are due to the different powder syntheses, which lead to different particle sizes and hence different micro structures and related variations in the density. The total ionic conductivity of 2.10^{-4} S/cm is comparable with polymer-based lithium electrolytes. Total ionic conductivity of these polymer-based electrolytes ranges from 10^{-3}–10^{-5} S/cm at room temperature (for instance [24,25]).

4. Discussion

4.1. Comparison of the SEM and XRD Results

Summarizing the SEM and XRD results leads to a trend between the grain size and the peak width. The difference in peak widths is probably caused only by the primary grain size, i.e., the smaller the primary grains the broader the XRD peaks. The primary particles causing peak broadening are the crystallites consisting of a coherently diffracting domain. The decrease in peak width of the statically compacted samples is caused by grain growth during the compaction process. The HUP BPO_4-Li_2O samples clearly show this grain growth which is caused by the high temperature during pressing. The CUP BPO_4-Li_2O samples also show a slight grain growth which indicates that applied pressures also activate grain growth.

The dynamically compacted BPO_4-Li_2O samples do not show any grain growth. The compaction time during explosive compaction is only a few micro-seconds and for magnetic pulse compaction about 200 μs. The process of dynamic compaction is too fast for grain growth to occur. In addition, dynamic compaction is a relatively low-temperature process.

4.2. Electrical Measurements

From the results of the electrical measurements it can be concluded that the total ionic conductivity increases with increasing compaction pressure or pressure wave velocity. Combined with the SEM and XRD results, a trend between the primary grain size and ionic conductivity can be derived: the total ionic conductivity increases with decreasing grain size. The total ionic conductivity consists of grain boundary and bulk conductivity. With the observed relation between grain size and total ionic conductivity it may be concluded that grain boundary conduction is the main conduction mechanism. This conclusion is supported by the fact that the dynamically compacted BPO_4-Li_2O samples have a higher concentration of grain boundaries than the statically compacted BPO_4-Li_2O samples due to a smaller grain size of the dynamically compacted material.

Accurate ac impedance analysis fitting will result in values for the bulk ionic conductivity and the grain boundary ionic conductivity, which will be combined with temperature dependent electrical measurements in future research.

4.3. Introduction of Lattice Defects During Dynamic Compaction

Introduction of one- or higher-dimensional lattice defects during dynamic compaction could also contribute to peak broadening. It was shown before [26] that explosive compaction can introduce one- and higher-dimensional lattice defects. In order to investigate the type and concentration of defects in the dynamically compacted BPO_4-Li_2O a quantitative series of XRD experiments will be complemented with transmission electron microscopy (TEM) and

high-resolution electron microscopy (HREM) analysis. Ongoing dynamic nuclear magnetic resonance (NMR) experiments on compacted BPO_4-Li_2O samples will result in the Li^+ mobility in the BPO_4-Li_2O lattice. From these data, combined with the Nernst–Einstein relation and accurate values of bulk ionic conductivities, the chemical diffusion coefficient can be calculated and the relevant lattice defect concentration can be cross-checked. These results will be published in a forthcoming paper.

5. Conclusions

Dynamic compaction is a suitable technique to compact BPO_4-Li_2O samples up to 75% of the theoretical mass density without altering the size of the nano- structured particles. The total ionic conductivity of dynamically compacted BPO_4-Li_2O can be up to three orders of magnitude higher compared to the total ionic conductivity of samples densified with static uniaxial pressing. The maximum measured total Li^+ conductivity of explosively compacted BPO_4-Li_2O samples is 2.10^{-4} S/cm at room temperature with grain boundary conductivity as the main conduction mechanism. This total ionic conductivity can compete with state-of-the-art polymer-based electrolytes.

Acknowledgments

References

1. F.R. Kalhammer, A. Kozawa, C.B. Moyer, and B.B. Owens, *J. Electrochem. Soc. Interface*, **5**, 32 (1996).

2. L.A. Dominey, in *Lithium Batteries* (Industrial Chemistry Library, Volume 5), G. Pistoia, Ed., p. 278, Elsevier Science, Amsterdam (1994).

3. Z.X. Shu, R.S. McMillan, and J.J. Murray, *J. Electrochem. Soc.*, **140**, L101 (1993).

4. Z. Jiang, M. Alamgir, and K.M. Abraham, *J. Electrochem. Soc.*, **142**, 333 (1995).

5. E.M. Kelder, M.J.G. Jak, F. de Lange, and J. Schoonman, *Solid State Ionics*, **85**, 285 (1996).

6. R.D. Shannon, B.E. Taylor, A.D. English, and T. Berzins, *Electrochem. Acta*, **22**, 783 (1977).

7. E.I. Burmakin, I.G. Sheckman, and G.K. Stepanov, *Sov. Electrochem.*, **18**, 248 (1982).

8. C.K. Lee and A.R. West, *J. Mater. Chem.*, **1**, 149 (1991).

9. R.A. Huggins, *Electrochem. Acta*, **22**, 773 (1977).

10. J.J. Carillo-Lazo, P. Quintana, and A. Huanosta, *Solid State Ionics*, **73**, 169 (1994).

11. A. Khorassani and A.R. West, *J. Solid State Chem.*, **53**, 369 (1984).

12. H. Aono, E. Sugimoto, N. Imanaka, and G. Adachi, *J. Electrochem. Soc.*, **137**, 1023 (1990).

13. J.B. Bates, N.J. Dudney, G.R. Gruzalski, R.A. Zuhr, A. Choudhury, C.F. Luck, and J.D. Robertson, *Solid State Ionics*, **53/56**, 647 (1992).

14. Xiaohua Yu, J.B. Bates, G.E. Jellison, Jr., and F.X. Hart, *J. Electrochem. Soc.*, **144**, 524 (1997).

15. M. Alamgir and K.M. Abraham, in *Lithium Batteries* Industrial Chemistry Library, Volume 5), G. Pistoia, Ed., p. 94–114, Elsevier Science, Amsterdam (1994).

16. M.J.G. Jak, E.M. Kelder, M. Stuivinga, and J. Schoonman, *Solid State Ionics*, **88**, 897 (1996).

17. M.J.G. Jak, E.M. Kelder, A.A. van Zomeren, and J. Schoonman, in *Exploratory Research and Development of Batteries for Electric and Hybrid Vehicles*, W.A. Adams, B. Scrosati, and A.R. Landgrebe, Eds., PV96-14, p. 58, The Electrochemical Society Proceedings Series, Pennington, NJ (1996).

18. G.E.R. Schulze, *Z. Physik. Chemie*, **B25**, 215 (1934).

19. E.A. Doroshkevisch and O.V. Roman, *Rep. 8th Union Powder Met. Conf.*, Minsk, 61 (1966).

20. J.D. Campbell, *Mater. Sci. Eng.*, **12**, 3 (1973).

21. J. Schoonman, in *The CRC Handbook of Solid State Electrochemistry*, P.J. Gellings and H.J.M. Bouwmeester, Eds., Chapter 5, CRC Press, Boca Raton (1997), p. 161–162..

22. J.Ross Macdonald (Ed.), *Impedance Spectroscopy*, Chapter 4, John Wiley & Sons, New York (1989), p. 231.

23. B.A. Boukamp, *Solid State Ionics*, **18/19**, 136 (1986).

24. G. Appetecchi, F. Croce, F. Gerace, S. Panero, S. Passerini, E. Spila, and B. Scrosati, in *Solid State Ionics IV*, G.A. Nazri, J.M. Tarascon, and M. Schreiber, Eds., **369**, p. 495, Mat. Res. Soc. Symp. Proc., Pittsburgh, Pennsylvania (1995).

25. E. Peled, D. Golodnitsky, G. Ardel, and A. Peled, in *Rechargeable Lithium and Lithium- Ion Batteries*, S. Megahed, B.M. Barnett, and L. Xie, Eds., **PV94-28**, p. 389, The Electrochemical Society Proceedings Series, Pennington, NJ (1995)..

26. D.K. Dijken, *Dynamic and Isostatic Densification of Powder Materials* (Ph.D. Thesis), University of Groningen, Chapter 6 (1994).